


Current-Perpendicular-to-Plane Giant Magnetoresistance Effect in van der Waals Heterostructures

Xinlu Li,¹ Yurong Su,² Meng Zhu,¹ Fanxing Zheng,¹ Peina Zhang,¹ Jia Zhang,^{1,*} and Jing-Tao Lü^{1,†}

¹*School of Physics and Wuhan National High Magnetic Field Center, Huazhong University of Science and Technology, 430074 Wuhan, China*

²*Department of Physics, Hubei University, Wuhan 430062, China*

 (Received 26 January 2021; revised 30 April 2021; accepted 3 September 2021; published 30 September 2021)

Spin-dependent transport in full van der Waals (vdW) giant magnetoresistance (GMR) junctions with the structure of $\text{Fe}_3\text{GeTe}_2/X\text{Te}_2/\text{Fe}_3\text{GeTe}_2$ ($X = \text{Pt}, \text{Pd}$) is investigated by using first-principles calculations. The ballistic conductance, magnetoresistance (MR), and resistance-area product (RA) are calculated in a current-perpendicular-to-plane (CPP) geometry. A giant magnetoresistance of around 2000% and RA less than $0.3 \Omega \mu\text{m}^2$ are found in the proposed vdW CPP GMR. In addition, the spin-orbit-coupling effect on transport and anisotropy magnetoresistance (AMR) are also investigated. The calculated AMR is found to be around 20% in the $\text{Fe}_3\text{GeTe}_2/\text{trilayer PdTe}_2/\text{Fe}_3\text{GeTe}_2$ CPP GMR. Both GMR and AMR in the proposed vdW CPP GMR mainly originate from the bulk electronic structure properties of Fe_3GeTe_2 . This work demonstrates a vdW CPP GMR with superior advantages, including perpendicular magnetic anisotropy, large GMR, low RA, and sizable AMR, which may stimulate future experimental explorations and should be appealing for its application in spintronic devices, including magnetic sensors and memory.

DOI: [10.1103/PhysRevApplied.16.034052](https://doi.org/10.1103/PhysRevApplied.16.034052)

I. INTRODUCTION

The giant magnetoresistance (GMR) effect in magnetic metallic multilayers was discovered by the groups of Fert [1] and Grünberg [2] in the 1980s. Since then, the metallic GMR structure, for instance, $[\text{Co}/\text{Cu}]_N$ multilayers, with a magnetoresistance ratio (MR) of more than 10% at room temperature, has been widely studied and applied in modern spintronic devices. For example, GMR is used as a read head in a hard disk drive (HDD) [3] and as a storage cell in magnetic random-access memory (MRAM) [4]. By replacing the nonmagnetic metallic spacer with a nanometer-thick insulating barrier, e.g., amorphous AlO_x [5], and later single-crystalline MgO barrier, the so-called magnetic tunnel junctions (MTJs) are shown to have a larger tunneling magnetoresistance (TMR), exceeding several-hundred percent at room temperature [6–10].

Nevertheless, for applications in next-generation higher density HDDs ($> 2 \text{ Tbit}/\text{in}^2$) and MRAM ($> 10 \text{ Gbit}/\text{in}^2$), there are significant challenges for conventional GMR and TMR junctions to satisfy the following criteria simultaneously [11,12]: (i) larger MR for high read-out signal, (ii) low resistance-area product (RA) for impedance matching and power-consumption reduction, (iii) perpendicular magnetic anisotropy of magnetic layers to achieve

faster magnetization switching and minimize stray fields between neighboring cells (and therefore, high area density) in MRAM. For example, for MRAM with a density of around $10 \text{ Gbit}/\text{in}^2$, it requires a storage cell that has $\text{RA} < 3.5 \Omega \mu\text{m}^2$ and $\text{MR} > 100\%$ [5], and for a HDD with an area density of $2 \text{ Tbit}/\text{in}^2$, it requires a similar MR but an order of magnitude smaller RA. Unfortunately, at present, neither GMR junctions nor MTJs can meet the above requirements. Metallic GMR junctions have a low RA, but the MR is also low (typically less than 100%). For TMR junctions, the MR is usually high enough, but the RA is inevitably large due to the electron-tunneling process across the insulating barrier. Those restrictions originate from the intrinsic electronic properties of conventional materials.

Stimulated by recently discovered van der Waals (vdW) materials, one may be able to build magnetic vdW heterostructures with appealing properties. Indeed, heterostructures based on magnetic vdW materials are revealed to have interesting functionalities. Recently, it has been reported that by using CrI_3 as a spin-filter barrier, graphite/ CrI_3 /graphite vdW tunnel junctions exhibit a record-high magnetoresistance over thousands of percent at low temperature [13–15]. Additionally, MTJs using Fe_3GeTe_2 as ferromagnetic electrodes have been investigated both experimentally [16] and theoretically [17,18]. Besides, a large TMR induced by the spin-filter effect is reported in transition-metal dichalcogenide MTJs [19].

*jiazhang@hust.edu.cn

†jtl@hust.edu.cn

Here, we build a full vdW GMR junction and consider the current-perpendicular-to-plane (CPP) transport geometry with a structure of $\text{Fe}_3\text{GeTe}_2/X\text{Te}_2/\text{Fe}_3\text{GeTe}_2$ ($X = \text{Pt}, \text{Pd}$) by using a type-II Dirac semimetal, $X\text{Te}_2$ ($X = \text{Pt}, \text{Pd}$) [20–24], as the nonmagnetic metallic spacer. Fe_3GeTe_2 is chosen as the magnetic electrode, since, among known two-dimensional (2D) ferromagnetic vdW metals, Fe_3GeTe_2 exhibits a relatively high Curie temperature of around 220 K [25–29] and can be further enhanced above room temperature by ionic gating [30]. In addition, since both PtTe_2 and PdTe_2 include heavy elements, the spin-orbit coupling may be sufficient to produce appreciable anisotropic transport phenomena. We investigate the ballistic transport phenomena, including giant magnetoresistance and anisotropic magnetoresistance effects in the proposed vdW CPP GMR by first-principles calculations.

II. CALCULATION METHODS

First-principles calculations are performed at the density-functional-theory level by using the generalized gradient approximation [31] of exchange-correlation potential and the ultrasoft pseudopotential [32], as implemented in Quantum ESPRESSO (QE) [33]. A Monkhorst-Pack k -point mesh of $12 \times 12 \times 1$ is used, and the cut-off energies for wave function and charge density are set to 40 and 320 Ry for self-consistent calculations of the $\text{Fe}_3\text{GeTe}_2/X\text{Te}_2/\text{Fe}_3\text{GeTe}_2$ ($X = \text{Pt}, \text{Pd}$) supercells. The vdW interaction is taken into account by employing the DFT-D3 scheme [34,35]. Before conducting electron-transport calculations of the CPP GMR, we calculate the magnetic crystalline anisotropy (MCA) energy of bulk Fe_3GeTe_2 by using force theorem by employing the Vienna *ab initio* simulation package (VASP) [36]. MCA in force theorem is defined as the band-energy difference between various magnetization orientations. To achieve converged MCA, a much denser k -point mesh of $20 \times 20 \times 5$ is adopted. The calculated MCA (defined as the energy difference between magnetization along the c and a axes) of bulk Fe_3GeTe_2 is around 1.03 meV/Fe, which agrees well with previous theoretical and experimental results [37,38], confirming that the vdW CPP GMR with the Fe_3GeTe_2 electrode should have a perpendicular-magnetization easy axis.

The interface atomic structure of the vdW CPP GMR is established by matching the (1×1) in-plane cell of $X\text{Te}_2$ ($X = \text{Pt}, \text{Pd}$) and Fe_3GeTe_2 electrodes due to the small lattice mismatch [39]. The in-plane lattice constant of the CPP GMR is fixed to the experimental in-plane lattice constant of Fe_3GeTe_2 ($a = b = 3.991 \text{ \AA}$). In heterostructures, the stacking configuration and interlayer distance between Fe_3GeTe_2 and PtTe_2 (PdTe_2) are adjusted to minimize the total energy. It is found that the interface atomic configurations have the most favorable energy when the Pt (Pd) and Te atoms in the interfacial PtTe_2 (PdTe_2) layer sit at

the same in-plane sites of Fe and Ge atoms, respectively, in the interfacial Fe_3GeTe_2 layer. (Please see Note 2 within the Supplemental Material for detailed total-energy calculations of various interface-stacking configurations [39].) The Fe_3GeTe_2 /trilayer $X\text{Te}_2/\text{Fe}_3\text{GeTe}_2$ ($X = \text{Pt}, \text{Pd}$) CPP GMR structure is shown in Fig. 1(a), and the atomic positions in the junctions are fully relaxed until the forces on each atom are less than $10^{-4} \text{ Ry}/a_B \approx 2.57 \text{ meV}/\text{\AA}$, where $1 \text{ Ry} = 13.6 \text{ eV}$ and $a_B = 0.529 \text{ \AA}$ is the Bohr radius. The equilibrium interlayer distance between Fe_3GeTe_2 and PtTe_2 (PdTe_2) is found to be 2.747 \AA (2.682 \AA), which is typical of vdW-type interface spacing.

After building the $\text{Fe}_3\text{GeTe}_2/X\text{Te}_2/\text{Fe}_3\text{GeTe}_2$ ($X = \text{Pt}, \text{Pd}$) junctions as a scattering region, self-consistent calculations of the Fe_3GeTe_2 electrode and scattering region are conducted separately. Then, the $\mathbf{k}_{\parallel} = (k_x, k_y)$ -resolved electron transmission is calculated by matching the wave functions of Fe_3GeTe_2 electrodes and the scattering region with the $200 \times 200 \mathbf{k}_{\parallel}$ mesh in the 2D Brillouin zone (BZ). The ballistic conductance of the CPP GMR can be obtained by summarizing the transmission over the 2D BZ based on the Landauer formula [40–42] as follows:

$$G = \frac{e^2}{h} \sum_{\mathbf{k}_{\parallel}} T(\mathbf{k}_{\parallel}), \quad (1)$$

where $T(\mathbf{k}_{\parallel})$ is the electron-transmission probability at the Fermi energy, \mathbf{k}_{\parallel} is the wave vector, e is the elementary charge, and h is Planck's constant. When the GMR is calculated in the absence of spin-orbit coupling (SOC), the conductance can be written in spin-resolved form as [9,10]

$$G_{\sigma} = \frac{e^2}{h} \sum_{\mathbf{k}_{\parallel}} T_{\sigma}(\mathbf{k}_{\parallel}), \quad (2)$$

where σ is the spin index.

When the anisotropic magnetoresistance (AMR) is studied in the presence of SOC, the Bloch states are no longer eigenstates of the spin operator and each Bloch state has mixed spin-up and spin-down components. Therefore, in this situation, the conductance for each magnetic configuration is calculated by Eq. (1). The RA of the CPP GMR can be evaluated from the calculated transmission by its definition [39].

III. RESULTS AND DISCUSSION

The crystal structures of bulk $X\text{Te}_2$ ($X = \text{Pt}/\text{Pd}$) and Fe_3GeTe_2 are shown in Figs. 1(a) and 1(b), respectively. Figure 1(c) depicts their first BZs. The band structures of bulk Fe_3GeTe_2 , PtTe_2 , and PdTe_2 along the Γ - A direction (transport direction) are shown in Figs. 1(d)–1(g). For Fe_3GeTe_2 , the spin-up band structure crossing the Fermi level belongs to Δ_1 symmetry, which is mainly composed

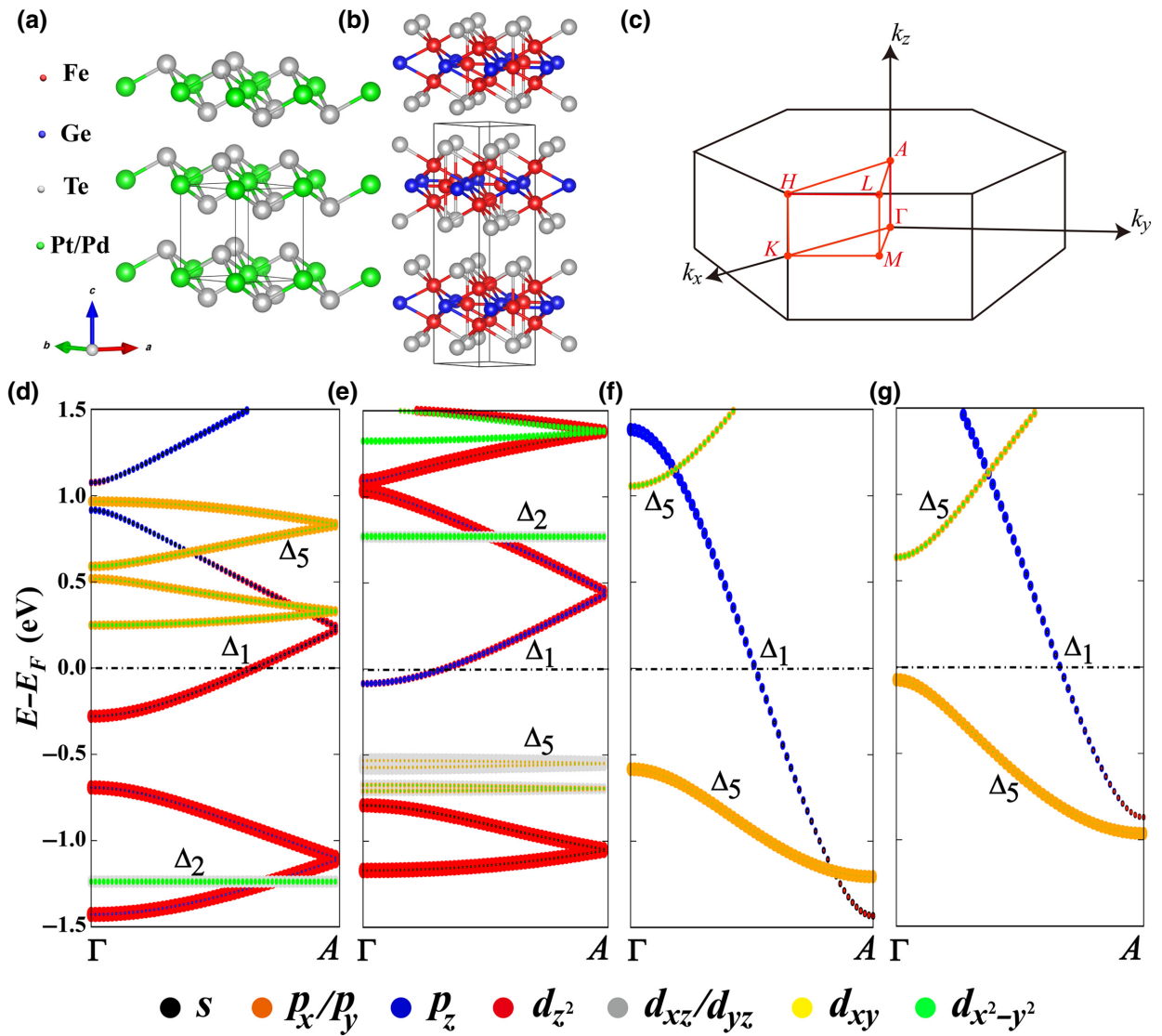


FIG. 1. (a),(b) Crystal structures of bulk $X\text{Te}_2$ ($X = \text{Pt/Pd}$) and Fe_3GeTe_2 . Black boxes in (a),(b) indicate the bulk unit cell. (c) Brillouin zone and high-symmetry \mathbf{k} path of a hexagonal lattice. (d),(e) Spin-up and spin-down band structures with orbital projections for Fe_3GeTe_2 along the Γ - A direction. (f),(g) Corresponding projected band structures for bulk PtTe_2 and PdTe_2 . Size of symbols in (d)–(g) is proportional to the projection weight of each orbital.

of the Fe d_z^2 orbital (see Fig. S2 in Note 4 within the Supplemental Material for atomic weight projections of band structures [39]). The spin-down band structure also has similar Δ_1 symmetry around the Fermi energy, which consists of Fe d_z^2 and Ge p_z orbitals. On the other hand, for PdTe_2 and PtTe_2 , the energy bands at the Fermi energy also have Δ_1 symmetry, which are mainly contributed to by the Te p_z orbital. In CPP transport geometry, the Bloch states with Δ_1 symmetry at the Fermi energy should have relatively large transmission due to its itinerant feature of the atomic orbital composition [9]. This agrees with the calculated results where transmissions around the $\bar{\Gamma}$ point are generally very large for both spin channels for

the $\text{Fe}_3\text{GeTe}_2/\text{trilayer } X\text{Te}_2/\text{Fe}_3\text{GeTe}_2$ ($X = \text{Pt, Pd}$) CPP GMR.

The 2D Fermi surfaces (FS) of electrodes, which indicate the distribution of available traveling Bloch states in the 2D BZ, play a decisive role in electron transport in the CPP GMR. Therefore, we calculate the 2D FS of bulk Fe_3GeTe_2 by calculating the transmission of identical $\text{Fe}_3\text{GeTe}_2/\text{Fe}_3\text{GeTe}_2/\text{Fe}_3\text{GeTe}_2$ sandwich structures. The calculated spin-polarized 2D FS of Fe_3GeTe_2 are shown in Figs. 2(b) and 2(c). By comparing Figs. 2(b) and 2(c), one can notice that the 2D FS for two spin channels are remarkably different. For spin-up channels, the Bloch states are available in most regions of the 2D BZ, while, for

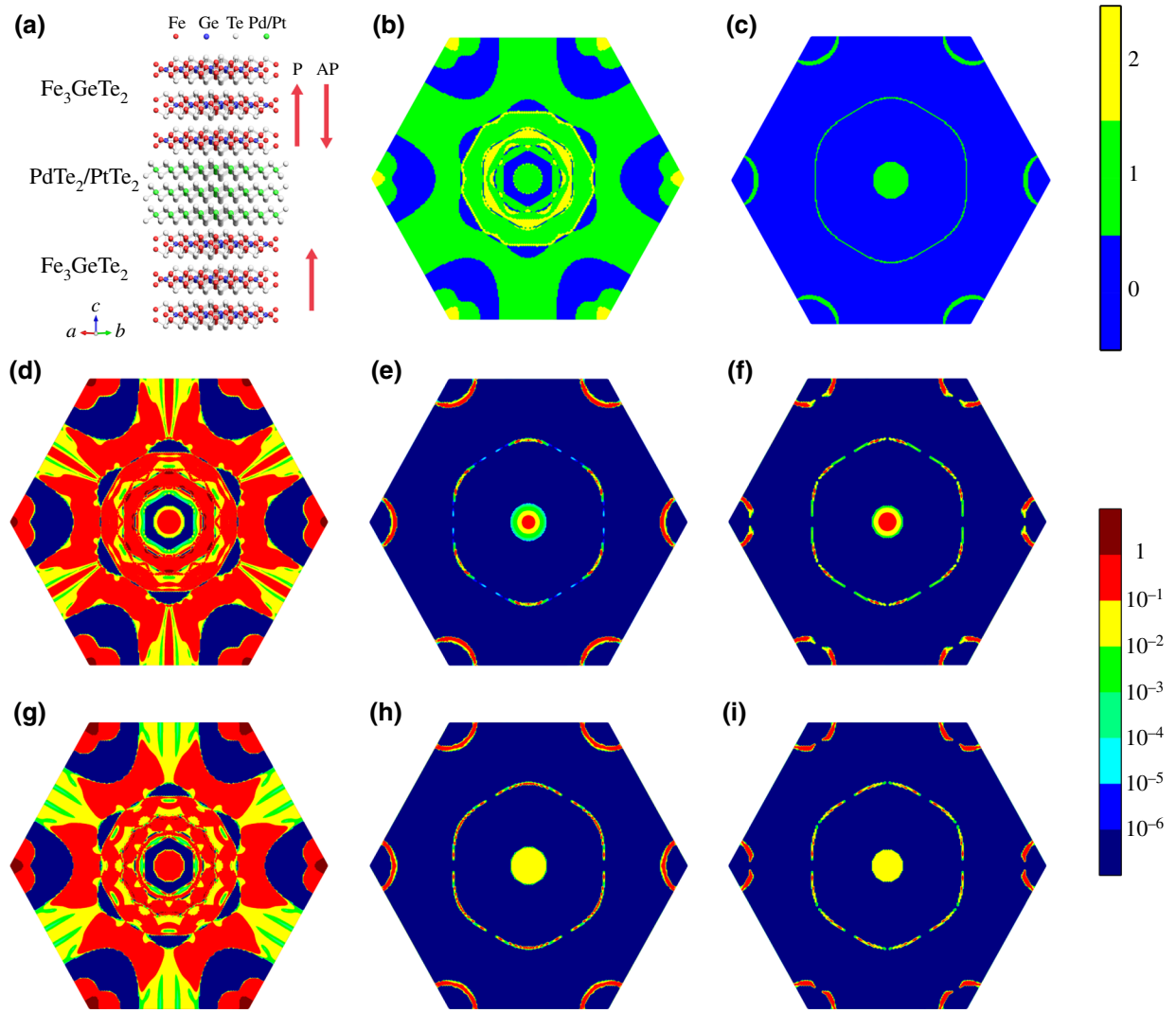


FIG. 2. (a) Atomic structure of Fe_3GeTe_2 /trilayer $X\text{Te}_2/\text{Fe}_3\text{GeTe}_2$ ($X = \text{Pt}, \text{Pd}$) CPP GMR. Red arrows indicate relative magnetization orientations of two Fe_3GeTe_2 electrodes. (b),(c) 2D FS of spin-up and spin-down channels for bulk Fe_3GeTe_2 . Color scale alongside (c) indicates the number of available Bloch states for two spin channels at each $\mathbf{k}_{\parallel} = (k_x, k_y)$ point. (d),(e) Spin-up and spin-down transmissions for Fe_3GeTe_2 /trilayer $\text{PdTe}_2/\text{Fe}_3\text{GeTe}_2$ CPP GMR for the parallel (P) configuration. (f) Transmission for the antiparallel (AP) configuration for spin-up (or spin-down) channels. (g)–(i) Same but for Fe_3GeTe_2 /trilayer $\text{PtTe}_2/\text{Fe}_3\text{GeTe}_2$ CPP GMR. Color scale alongside (f),(i) indicates the magnitude of transmissions shown for (d)–(i) on a logarithmic scale.

spin-down channels, only a small area around $\bar{\Gamma}(k_x = 0, k_y = 0)$ and \bar{K} points have available Bloch states. Such largely mismatched and highly spin-polarized 2D FS between two spin channels would greatly reduce transmission for the antiparallel magnetization configuration, which might instead ensure a high GMR ratio in the proposed vdW CPP GMR.

An illustration of the atomic structure of the Fe_3GeTe_2 /trilayer $X\text{Te}_2/\text{Fe}_3\text{GeTe}_2$ ($X = \text{Pt}, \text{Pd}$) CPP GMR is shown in Fig. 2(a). We then explicitly calculate electron transmission in the CPP GMR junctions for P and AP magnetization configurations of two Fe_3GeTe_2 electrodes. As seen in Figs. 2(d)–2(i), electron transmissions for spin-up and

spin-down channels generally resemble the shape of corresponding 2D FS of Fe_3GeTe_2 [Figs. 2(b) and 2(c)] but with modulated transmission at each \mathbf{k}_{\parallel} point. For instance, the transmission of the spin-up electron for the P configuration is consistent with the spin-up 2D FS [Fig. 2(b)], and the transmission of the spin-down electron for the P configuration and the transmission for the AP configuration [Figs. 2(f) and 2(i)] agree with the 2D FS of spin-down channels shown in Fig. 2(c). In a large area of the 2D BZ, the transmissions of spin-up channels for the P configuration are larger than 0.1, which results in a much larger total transmission (conductance) than that for the AP configurations. In addition, the band symmetry of electrons in the

TABLE I. Calculated spin-dependent electron transmissions T_{\uparrow} and T_{\downarrow} , RA for P and AP magnetization alignments of two Fe_3GeTe_2 layers, and the GMR ratio in the $\text{Fe}_3\text{GeTe}_2/\text{trilayer } X\text{Te}_2/\text{Fe}_3\text{GeTe}_2$ ($X = \text{Pt, Pd}$) vdW CPP GMR.

	$M_{\uparrow\uparrow}$ (parallel magnetization)			RA ($\text{m}\Omega\mu\text{m}^2$)	$M_{\uparrow\downarrow}$ (antiparallel magnetization)			GMR ratio (%)
	Spin-up T_{\uparrow}	Spin-down T_{\downarrow}	$T (=T_{\uparrow} + T_{\downarrow})$		Spin-up $T_{\uparrow}/\text{spin-down } T_{\downarrow}$	$T (=T_{\uparrow} + T_{\downarrow})$	RA ($\text{m}\Omega\mu\text{m}^2$)	
Trilayer PtTe_2	3.25×10^{-1}	8.99×10^{-3}	3.34×10^{-1}	10.7	8.04×10^{-3}	1.60×10^{-2}	222.5	1979
Trilayer PdTe_2	3.25×10^{-1}	9.07×10^{-3}	3.34×10^{-1}	10.7	8.28×10^{-3}	1.66×10^{-2}	214.5	1905

electrodes at each \mathbf{k}_{\parallel} point is also important for determining transmission through the CPP GMR.

The calculated electron transmissions, RA, and the corresponding GMR ratio (defined as $[(G_{\text{P}}/G_{\text{AP}}) - 1] \times 100\%$, where G_{P} and G_{AP} are the conductance for P and AP magnetic configurations, respectively) for the $\text{Fe}_3\text{GeTe}_2/\text{trilayer } X\text{Te}_2/\text{Fe}_3\text{GeTe}_2$ ($X = \text{Pt, Pd}$) CPP GMR are listed in Table I. We ignore the SOC effect when the GMR is investigated (see Note 6 within the Supplemental Material for discussions of the SOC effect on the GMR [39]), since the GMR ratio mainly depends on the relative magnetization orientations and the spin-polarized band structures of the two magnetic electrodes. Generally, a GMR ratio of around 2000% and RA of less than $0.3 \Omega\mu\text{m}^2$ are obtained in the proposed vdW CPP GMR. In comparison to the previously studied $\text{Fe}_3\text{GeTe}_2/\text{graphene}/\text{Fe}_3\text{GeTe}_2$ tunneling magnetoresistance structure, where RA is around $5 \Omega\mu\text{m}^2$ [17], it suggests that the proposed metallic CPP GMR with low RA and high magnetoresistance may be more promising for device applications. It is worth noting that the transport properties in the CPP GMR do not change significantly by using either trilayer PtTe_2 or trilayer PdTe_2 as metallic spacer layers. This is not surprising, since the interface interactions between the Fe_3GeTe_2 electrode and spacer layers are of weak vdW type, which makes the transport properties of the CPP GMR mostly determined by the Fe_3GeTe_2 electrode rather than spacer layers and the interfaces. As a consequence, the large GMR ratio in this class of vdW CPP GMR can be mainly attributed to the highly spin-polarized electronic structures of Fe_3GeTe_2 , which is the significantly distinct 2D FS for two spins discussed above.

The origin of the large GMR ratio in the studied vdW CPP GMR differs from that in conventional GMR

multilayer structures. For GMR multilayer structures, both the bulk and interface spin-dependent scattering are crucial [43]. Typically, the experimentally reported GMR ratio of conventional $[\text{Co}/\text{Cu}]_N$ and $[\text{Fe}/\text{Cr}]_N$ multilayers is around tens of percent at room temperature [44,45]. Besides, in a conventional CPP GMR using high-spin-polarized Heusler alloys as magnetic electrodes, the GMR ratio can be further enhanced [46–48]. In Table II, we list the GMR ratios and RAs for typical conventional CPP GMR structures. The largest GMR ratio obtained in the CPP GMR with Heusler alloy electrodes is found to be around 73% at room temperature; this is attributed to enhanced interfacial-spin-asymmetry scattering [48].

Recently, 2D materials have also been adopted in CPP GMRs. For example, in the $\text{Fe}/\text{MoS}_2/\text{Fe}$ CPP GMR, with the transition-metal dichalcogenide semiconductor MoS_2 as a spacer layer, first-principles calculations predict a GMR ratio up to 300% [51]. Experimentally, the GMR ratio is reported to be less than 1% at low temperature ($T = 10$ K) and with an extremely large RA of around $100 \Omega\mu\text{m}^2$ in the $\text{NiFe}/\text{MoS}_2/\text{NiFe}$ CPP GMR [49]. More recently, a vdW CPP GMR with a structure of $\text{Fe}_3\text{GeTe}_2/\text{MoS}_2/\text{Fe}_3\text{GeTe}_2$ has also been experimentally fabricated, and the GMR ratio is found to be around 3.1% at 10 K [50]. The achieved low experimental GMR ratio in such a CPP GMR with MoS_2 as a spacer layer may be attributed to several reasons. First, although contact between the magnetic electrodes and MoS_2 spacer is metallic due to strong interface hybridization, the resultant RA should be large, since much fewer energy bands are present at the Fermi level compared with metallic spacers like PtTe_2 and PdTe_2 . Second, a semiconductor may not be a good spacer-layer candidate for a GMR, since the metal-semiconductor contact may not be ideal and could

TABLE II. Experimental RA, ΔRA [defined as $(\text{RA})_{\text{AP}} - (\text{RA})_{\text{P}}$], and GMR ratio for typical CPP GMRs.

Structures of CPP GMR	RA ($\text{m}\Omega\mu\text{m}^2$)	ΔRA ($\text{m}\Omega\mu\text{m}^2$)	GMR ratio (%)	Refs.
$[\text{Co}/\text{Cu}]_{180}; [\text{Fe}/\text{Cr}]_{100}$	–	–	56; 14 ($T = 300$ K)	[45]
$\text{Co}_2\text{Fe}_{0.4}\text{Mn}_{0.6}\text{Si}/\text{Ag}/\text{Co}_2\text{Fe}_{0.4}\text{Mn}_{0.6}\text{Si}$	17.2–369.2 (AP state)	–	62–75% ($T = 300$ K)	[47]
$\text{Co}_2\text{Fe}_{0.4}\text{Mn}_{0.6}\text{Si}/\text{Ag-Mg}/\text{Co}_2\text{Fe}_{0.4}\text{Mn}_{0.6}\text{Si}$	37 (P state)	27	73 ($T = 300$ K)	[48]
$\text{NiFe}/\text{MoS}_2/\text{NiFe}$	$\sim 10^5$	–	0.4 ($T = 10$ K)	[49]
$\text{Fe}_3\text{GeTe}_2/\text{MoS}_2/\text{Fe}_3\text{GeTe}_2$	–	841.9	3.1 ($T = 10$ K)	[50]

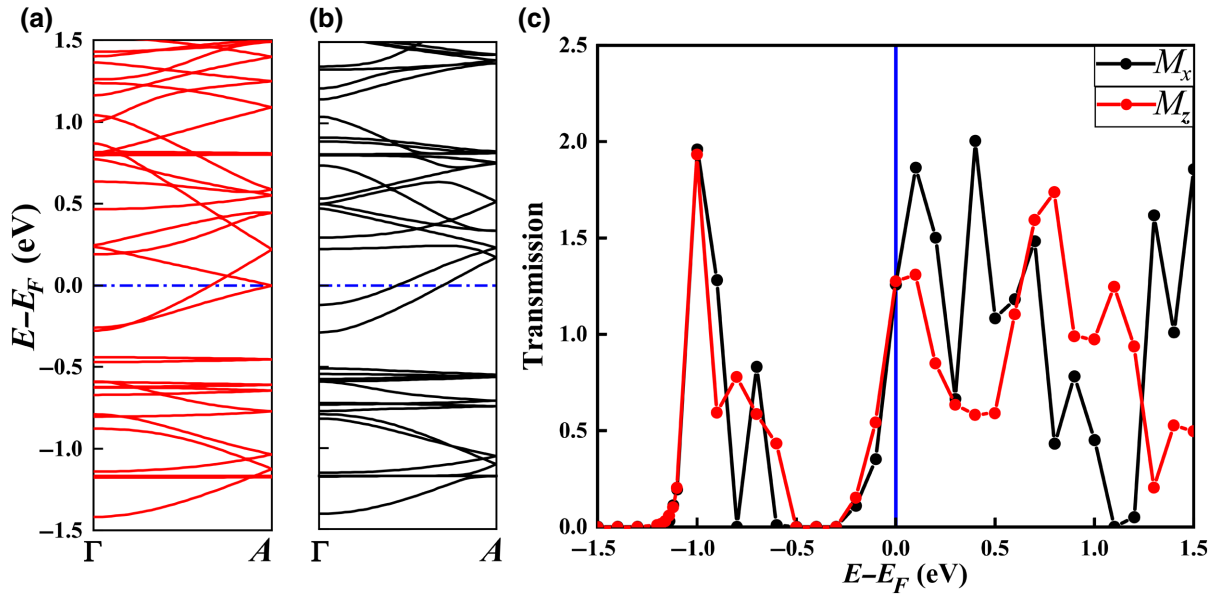


FIG. 3. (a),(b) Energy-band structures of bulk Fe_3GeTe_2 along the Γ - A direction for M_z (red lines) and M_x (black lines) magnetization states. (c) Transmission of the Fe_3GeTe_2 /trilayer $\text{PdTe}_2/\text{Fe}_3\text{GeTe}_2$ CPP GMR as a function of energy at $\mathbf{k}_{\parallel} = (0,0)$ for M_z and M_x cases. Fermi energy is set to zero. Notably, over some energy ranges, transmission is larger than one, since more than one Bloch state is present at the corresponding energy.

produce a Fermi-energy pinning effect [52], which is detrimental for spin-dependent transport.

Experimentally, the crystal structure in vdW heterostructures may not be perfect because of the weak interlayer interaction. For example, there may be interlayer misalignments and relative rotations between the Fe_3GeTe_2 electrode and PtTe_2 (PdTe_2) spacer layer. Such structural imperfections may impact on the transport properties in the studied vdW CPP GMR. Our previous theoretical model [17] shows that the magnetoresistance has a weak dependence on interlayer translation, while an order of magnitude decrease in magnetoresistance is found when the relative rotation of the two Fe_3GeTe_2 electrodes occurs. At finite temperature, the GMR ratio may decrease with an increase of temperature because of the demagnetization of magnetic vdW electrodes and possible spin-flipped scattering by magnons. As we discussed previously, the electronic structures of the magnetic electrode will mainly determine the GMR ratio. Therefore, the key for achieving a high experimental GMR value in vdW magnetic heterostructures at finite temperature is to explore vdW ferromagnetic materials with Curie temperatures well above room temperature and high spin polarization (ideally half-metallic ferromagnets with only one type of conducting spin channels at the Fermi energy).

The SOC effect plays an essential role in the appearance of topological band structures of Fe_3GeTe_2 and $X\text{Te}_2$ ($X = \text{Pd}, \text{Pt}$) and the triggering magnetic anisotropy of Fe_3GeTe_2 . For example, when SOC is taken into account, Fe_3GeTe_2 is found to be a nodal line semimetal [28] and

$X\text{Te}_2$ ($X = \text{Pd}, \text{Pt}$) are type-II Dirac semimetals [20–22]. Spin-orbit coupling may also have a notable impact on electron transport in the proposed vdW CPP GMR and produce anisotropic conductance dependent on the magnetization orientations of Fe_3GeTe_2 .

The band structures of Fe_3GeTe_2 along the Γ - A high-symmetry line (parallel to the transport direction) for M_z and M_x cases are shown in Figs. 3(a) and 3(b). It is clear that the band dispersion is strongly coupled to the magnetization orientation due to the sizable SOC effect in Fe_3GeTe_2 . A similar magnetization direction dependence of the band structures in Fe_3GeTe_2 along other high-symmetry lines, for instance, M - K , K - Γ , and Γ - H in the Brillouin zone has also been theoretically discussed [28]. Consequently, the Bloch states of Fe_3GeTe_2 at each \mathbf{k}_{\parallel} point in the 2D BZ possess different band features like crystal momentum k_z and electron velocity v_z along the transport direction for the M_z and M_x cases, which leads to an anisotropic transmission probability in the CPP GMR. We also investigate the AMR effect of the Fe_3GeTe_2 /trilayer $\text{PdTe}_2/\text{Fe}_3\text{GeTe}_2$ CPP GMR by calculating electron transmission in the presence of SOC when the magnetization directions of two Fe_3GeTe_2 electrodes are fixed to be parallel but rotate simultaneously along the z and x directions. Details of the transport calculations in the presence of SOC can be found in Note 7 within the Supplemental Material [39]. Transmission of the CPP GMR at the $\bar{\Gamma}$ point as a function of energy is calculated and shown in Fig. 3(c). It is clear that, in a wide-energy window, the transmissions for M_z and M_x

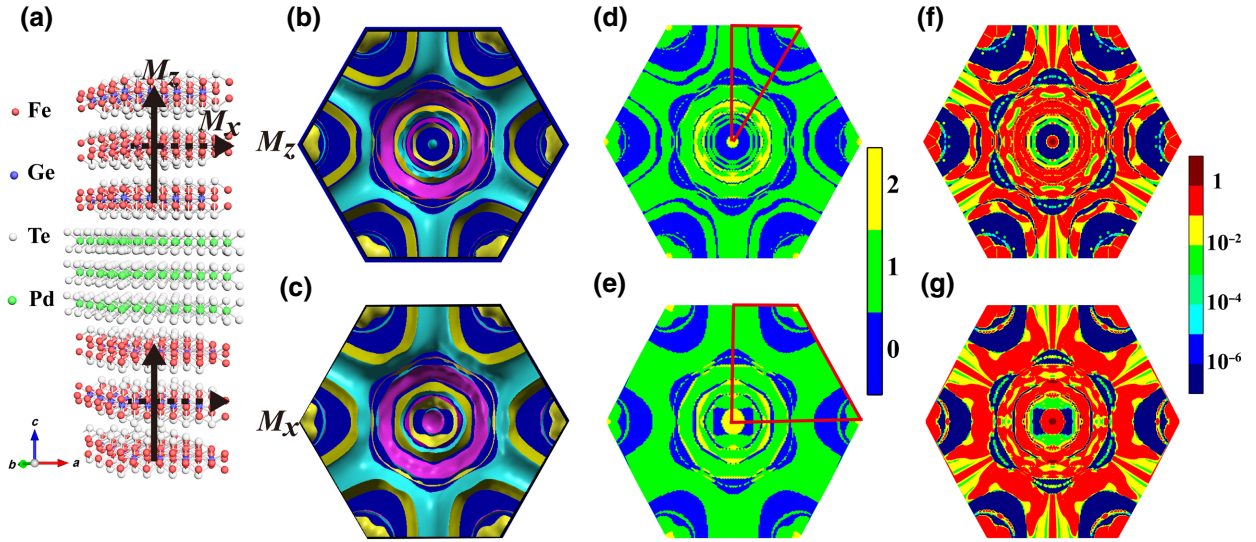


FIG. 4. (a) Atomic structure of the Fe_3GeTe_2 /trilayer $\text{PdTe}_2/\text{Fe}_3\text{GeTe}_2$ CPP GMR. Black arrows indicate magnetization directions of two Fe_3GeTe_2 electrodes. Top view of 3D FS (b),(c); 2D FS (d),(e) of bulk Fe_3GeTe_2 ; and electron-transmission distribution of CPP GMR (f),(g) in the presence of SOC for M_z and M_x cases. Colors in (b),(c) indicate Fermi surfaces belonging to different bands. Red frames in (d),(e) show the irreducible BZ for calculating 2D FS and transmission. Color scales along the side of (d),(e) and (f),(g) indicate available Bloch states and transmission, respectively.

are remarkably different. Especially, for an energy slightly above the Fermi energy, a stronger anisotropic transmission is present, which indicates a possible larger AMR at that energy window.

Similarly, prior to calculating the transmission, we calculate and plot the three-dimensional (3D) FS of bulk Fe_3GeTe_2 for magnetization along the z (M_z) and x (M_x) axes. The 3D FS of Fe_3GeTe_2 are shown in Figs. 4(b) and 4(c), which exhibit different \mathbf{k} symmetry in the BZ. For the M_z case, the magnetic point group of Fe_3GeTe_2 is D_{6h} ($6/mmm$), which has 24 symmetry operations in total, while, for the M_x case, the magnetic point group belongs to D_{2h} (mmm) with lower symmetry. The irreducible 2D BZs where transmission is explicitly calculated for M_z and M_x cases are indicated by the red frames shown in Figs. 4(d) and 4(e). Most importantly, the 2D FS for the M_z case [Fig. 4(d)] covers less area than the M_x case [Fig. 4(e)] around the $\bar{\Gamma}$ point. As we have discussed previously, the Bloch states with Δ_1 band symmetry around the $\bar{\Gamma}$ points should have relatively large transmission, as shown in Figs. 4(f) and 4(g). As a consequence, evaluation of the FS around the $\bar{\Gamma}$ point by rotating magnetization of Fe_3GeTe_2 leads to an anisotropic conductance and a larger total transmission for M_x than that for the M_z case.

The calculated transmission, RA, and AMR ratio (defined as $\{[G(M_x)/G(M_z)] - 1\} \times 100\%$) in the Fe_3GeTe_2 /trilayer $\text{PdTe}_2/\text{Fe}_3\text{GeTe}_2$ CPP GMR are listed in Table III. Transmission of the CPP GMR for the M_x case is larger than that for the M_z case, which leads to an AMR of around 20%. The origin of AMR in the vdW CPP GMR can also be mainly attributed to

bulk electronic structure evaluation of Fe_3GeTe_2 for different magnetization orientations, as we have discussed previously. In contrast, the origin of AMR is different from that in a conventional AMR structure. For instance, in magnetic tunnel junctions, the tunneling anisotropic magnetoresistance generally originates from the surface and interface resonant states [53,54]. Recently, an anti-symmetric magnetoresistance effect has been reported in Fe_3GeTe_2 /Graphite/ Fe_3GeTe_2 trilayer heterostructures in a current-in-plane geometry that originates from a different mechanism. The spin-momentum-locking-induced spin-polarized current at the graphite/ Fe_3GeTe_2 interface is found to be responsible for the presence of MR in this system [55].

The full vdW heterostructures proposed in this work should be fabricated more easily and retain better crystal quality with fewer interface defects, including interface alloys and surface roughness, in comparison with a traditional CPP GMR. In the proposed CPP GMR, parallel and antiparallel magnetic orientations of two Fe_3GeTe_2 electrodes can be realized by employing different coercivities of two Fe_3GeTe_2 layers by layer-thickness and film-shape

TABLE III. Calculated electron transmission, RA, and AMR in the Fe_3GeTe_2 /trilayer $\text{PdTe}_2/\text{Fe}_3\text{GeTe}_2$ CPP GMR.

	M_z		M_x		
	RA		RA		
Transmission ($\text{m}\Omega \mu\text{m}^2$)	Transmission ($\text{m}\Omega \mu\text{m}^2$)		Transmission ($\text{m}\Omega \mu\text{m}^2$)		AMR (%)
2.20×10^{-1}	16.18	2.65×10^{-1}	13.43		20.5

engineering. An alternative way to realize the P and AP states of the CPP GMR is to pin one of the Fe_3GeTe_2 layers with an adjacent antiferromagnetic layer [56,57]. In the case of anisotropic magnetoresistance, different magnetic moment orientations of two Fe_3GeTe_2 can be achieved by applying a sufficiently large magnetic field along various directions [54].

IV. SUMMARY

Spin-dependent transport properties in a full vdW CPP GMR with the structure of $\text{Fe}_3\text{GeTe}_2/\text{trilayer } X\text{Te}_2/\text{Fe}_3\text{GeTe}_2$ ($X = \text{Pt}, \text{Pd}$) are studied by employing first-principles calculations. A giant GMR ratio of around 2000%, a low RA of less than $0.3 \Omega \mu\text{m}^2$, and perpendicular magnetization anisotropy are predicted simultaneously in those vdW metallic CPP GMRs. When spin-orbit coupling is taken into account, the $\text{Fe}_3\text{GeTe}_2/\text{trilayer PdTe}_2/\text{Fe}_3\text{GeTe}_2$ CPP GMR is found to have an AMR value of around 20%. The mechanism for the GMR effect in the studied vdW CPP GMR mainly relies on the spin-polarized electronic structure of the ferromagnetic Fe_3GeTe_2 electrodes, whereas the AMR effect originates from the anisotropic electronic structure of Fe_3GeTe_2 along different magnetization directions. Our calculation results demonstrate that the proposed vdW CPP GMR, with perpendicular magnetic anisotropy, a giant GMR ratio, low RA, and moderate AMR, should be promising for device applications, including magnetic sensors and memory. This work may stimulate future experimental explorations of the magnetoresistance effect in vdW-type CPP GMRs.

ACKNOWLEDGMENTS

J.Z. and J.-T.L. acknowledge support from the National Natural Science Foundation of China (Grants No. 11704135 and No. 21873033), program for the HUST academic frontier youth team. The computations in this work are partly performed on the Platform for Data-Driven Computational Materials Discovery at Songshan Lake Materials Laboratory, Dongguan, China.

[1] M. N. Baibich, J. M. Broto, A. Fert, F. Nguyen Van Dau, F. Petroff, P. Etienne, G. Creuzet, A. Friederich, and J. Chazelas, Giant Magnetoresistance of (001)Fe/(001)Cr Magnetic Superlattices, *Phys. Rev. Lett.* **61**, 2472 (1988).
 [2] G. Binasch, P. Grünberg, F. Saurenbach, and W. Zinn, Enhanced magnetoresistance in layered magnetic structures with antiferromagnetic interlayer exchange, *Phys. Rev. B* **39**, 4828 (1989).
 [3] A. Hirohata and K. Takanashi, Future perspectives for spintronic devices, *J. Phys. D: Appl. Phys.* **47**, 193001 (2014).

[4] S. Bhatti, R. Sbiaa, A. Hirohata, H. Ohno, S. Fukami, and S. N. Piramanayagam, Spintronics based random access memory: A review, *Mater. Today* **20**, 530 (2017).
 [5] H. X. Wei, Q. H. Qin, M. Ma, R. Sharif, and X. F. Han, 80% tunneling magnetoresistance at room temperature for thin Al–O barrier magnetic tunnel junction with CoFeB as free and reference layers, *J. Appl. Phys.* **101**, 09B501 (2007).
 [6] S. S. Parkin, C. Kaiser, A. Panchula, P. M. Rice, B. Hughes, M. Samant, and S. H. Yang, Giant tunnelling magnetoresistance at room temperature with MgO (100) tunnel barriers, *Nat. Mater.* **3**, 862 (2004).
 [7] S. Yuasa, T. Nagahama, A. Fukushima, Y. Suzuki, and K. Ando, Giant room-temperature magnetoresistance in single-crystal Fe/MgO/Fe magnetic tunnel junctions, *Nat. Mater.* **3**, 868 (2004).
 [8] S. Ikeda, J. Hayakawa, Y. Ashizawa, Y. M. Lee, K. Miura, H. Hasegawa, M. Tsunoda, F. Matsukura, and H. Ohno, Tunnel magnetoresistance of 604% at 300 K by suppression of Ta diffusion in CoFeB/MgO/CoFeB pseudo-spin-valves annealed at high temperature, *Appl. Phys. Lett.* **93**, 082508 (2008).
 [9] W. H. Butler, X. G. Zhang, T. C. Schulthess, and J. M. MacLaren, Spin-dependent tunneling conductance of Fe|MgO|Fe sandwiches, *Phys. Rev. B* **63**, 054416 (2001).
 [10] J. Mathon and A. Umerski, Theory of tunneling magnetoresistance of an epitaxial Fe/MgO/Fe(001) junction, *Phys. Rev. B* **63**, 220403(R) (2001).
 [11] M. Takagishi, K. Yamada, H. Iwasaki, H. N. Fuke, and S. Hashimoto, Magnetoresistance ratio and resistance area design of CPP-MR film for 2–5 Tb/in² read sensors, *IEEE Trans. Magn.* **46**, 2086 (2010).
 [12] A. Hirohata, W. Frost, M. Samiepour, and J. Y. Kim, Perpendicular magnetic anisotropy in Heusler alloy films and their magnetoresistive junctions, *Materials* **11**, 105 (2018).
 [13] T. Song, X. Cai, M. W.-Y. Tu, X. Zhang, B. Huang, N. P. Wilson, K. L. Seyler, L. Zhu, T. Taniguchi, and K. Watanabe, Giant tunneling magnetoresistance in spin-filter van der Waals heterostructures, *Science* **360**, 1214 (2018).
 [14] D. R. Klein, D. MacNeill, J. L. Lado, D. Soriano, E. Navarro-Moratalla, K. Watanabe, T. Taniguchi, S. Manni, P. Canfield, and J. Fernández-Rossier, Probing magnetism in 2D van der Waals crystalline insulators via electron tunneling, *Science* **360**, 1218 (2018).
 [15] Z. Wang, I. Gutierrez-Lezama, N. Ubrig, M. Kroner, M. Gibertini, T. Taniguchi, K. Watanabe, A. Imamoglu, E. Giannini, and A. F. Morpurgo, Very large tunneling magnetoresistance in layered magnetic semiconductor CrI_3 , *Nat. Commun.* **9**, 2516 (2018).
 [16] Z. Wang, D. Sapkota, T. Taniguchi, K. Watanabe, D. Mandrus, and A. F. Morpurgo, Tunneling spin valves based on $\text{Fe}_3\text{GeTe}_2/\text{hBN}/\text{Fe}_3\text{GeTe}_2$ van der Waals heterostructures, *Nano Lett.* **18**, 4303 (2018).
 [17] X. L. Li, J. T. Lu, J. Zhang, L. You, Y. R. Su, and E. Y. Tsymbal, Spin-dependent transport in van der Waals magnetic tunnel junctions with Fe_3GeTe_2 electrodes, *Nano Lett.* **19**, 5133 (2019).
 [18] L. Zhang, T. Li, J. Li, Y. Jiang, J. Yuan, and H. Li, Perfect spin filtering effect on Fe_3GeTe_2 -based van der Waals magnetic tunnel junctions, *J. Phys. Chem. C* **124**, 27429 (2020).

- [19] W. Yang, Y. Cao, J. Han, X. Lin, X. Wang, G. Wei, L. Chen, A. Bournel, and W. Zhao, Spin-filter induced large magnetoresistance in 2D van der Waals magnetic tunnel junctions, *Nanoscale* **13**, 862 (2021).
- [20] H. Huang, S. Zhou, and W. Duan, Type-II Dirac fermions in the PtSe₂ class of transition metal dichalcogenides, *Phys. Rev. B* **94**, 121117(R) (2016).
- [21] M. Yan, H. Huang, K. Zhang, E. Wang, W. Yao, K. Deng, G. Wan, H. Zhang, M. Arita, H. Yang, Z. Sun, H. Yao, Y. Wu, S. Fan, W. Duan, and S. Zhou, Lorentz-violating type-II Dirac fermions in transition metal dichalcogenide PtTe₂, *Nat. Commun.* **8**, 257 (2017).
- [22] F. Fei, X. Bo, R. Wang, B. Wu, J. Jiang, D. Fu, M. Gao, H. Zheng, Y. Chen, X. Wang, H. Bu, F. Song, X. Wan, B. Wang, and G. Wang, Nontrivial Berry phase and type-II Dirac transport in the layered material PdTe₂, *Phys. Rev. B* **96**, 041201(R) (2017).
- [23] K. Zhang, M. Yan, H. Zhang, H. Huang, M. Arita, Z. Sun, W. Duan, Y. Wu, and S. Zhou, Experimental evidence for type-II semimetal in PtSe₂, *Phys. Rev. B* **96**, 125102 (2017).
- [24] H. J. Noh, J. Jeong, E. J. Cho, K. Kim, B. I. Min, and B. G. Park, Experimental Realization of Type-II Dirac Fermions in a PdTe₂ Superconductor, *Phys. Rev. Lett.* **119**, 016401 (2017).
- [25] H. J. Deiseroth, K. Aleksandrov, C. Reiner, L. Kienle, and R. K. Kremer, Fe₃GeTe₂ and Ni₃GeTe₂ – two new layered transition-metal compounds: Crystal structures, HRTEM investigations, and magnetic and electrical properties, *Eur. J. Inorg. Chem.* **2006**, 1561 (2006).
- [26] B. Chen, J. Yang, H. Wang, M. Imai, H. Ohta, C. Michioka, K. Yoshimura, and M. Fang, Magnetic properties of layered itinerant electron ferromagnet Fe₃GeTe₂, *J. Phys. Soc. Jpn.* **82**, 124711 (2013).
- [27] Q. Li, *et al.*, Patterning-induced ferromagnetism of Fe₃GeTe₂ van der Waals materials beyond room temperature, *Nano Lett.* **18**, 5974 (2018).
- [28] K. Kim, J. Seo, E. Lee, K. T. Ko, B. S. Kim, B. G. Jang, J. M. Ok, J. Lee, Y. J. Jo, W. Kang, J. H. Shim, C. Kim, H. W. Yeom, B. Il Min, B. J. Yang, and J. S. Kim, Large anomalous Hall current induced by topological nodal lines in a ferromagnetic van der Waals semimetal, *Nat. Mater.* **17**, 794 (2018).
- [29] J. Seo, D. Y. Kim, E. S. An, K. Kim, G. Y. Kim, S. Y. Hwang, D. W. Kim, B. G. Jang, H. Kim, and G. Eom, Nearly room temperature ferromagnetism in a magnetic metal-rich van der Waals metal, *Sci. Adv.* **6**, eaay8912 (2020).
- [30] Y. Deng, Y. Yu, Y. Song, J. Zhang, N. Z. Wang, Z. Sun, Y. Yi, Y. Z. Wu, S. Wu, J. Zhu, J. Wang, X. H. Chen, and Y. Zhang, Gate-tunable room-temperature ferromagnetism in two-dimensional Fe₃GeTe₂, *Nature* **563**, 94 (2018).
- [31] J. P. Perdew, K. Burke, and M. Ernzerhof, Generalized Gradient Approximation Made Simple, *Phys. Rev. Lett.* **77**, 3865 (1996).
- [32] D. Vanderbilt, Soft self-consistent pseudopotentials in a generalized eigenvalue formalism, *Phys. Rev. B* **41**, 7892 (1990).
- [33] P. Giannozzi, *et al.*, Advanced capabilities for materials modelling with Quantum ESPRESSO, *J. Phys. Condens. Matter* **29**, 465901 (2017).
- [34] K. F. Garrity, J. W. Bennett, K. M. Rabe, and D. Vanderbilt, Pseudopotentials for high-throughput DFT calculations, *Comput. Mater. Sci.* **81**, 446 (2014).
- [35] S. Grimme, J. Antony, S. Ehrlich, and H. Krieg, A consistent and accurate ab initio parametrization of density functional dispersion correction (DFT-D) for the 94 elements H-Pu, *J. Chem. Phys.* **132**, 154104 (2010).
- [36] G. Kresse and J. Furthmüller, Efficiency of ab-initio total energy calculations for metals and semiconductors using a plane-wave basis set, *Comput. Mater. Sci.* **6**, 15 (1996).
- [37] H. L. Zhuang, P. R. C. Kent, and R. G. Hennig, Strong anisotropy and magnetostriction in the two-dimensional Stoner ferromagnet Fe₃GeTe₂, *Phys. Rev. B* **93**, 134407 (2016).
- [38] N. León-Brito, E. D. Bauer, F. Ronning, J. D. Thompson, and R. Movshovich, Magnetic microstructure and magnetic properties of uniaxial itinerant ferromagnet Fe₃GeTe₂, *J. Appl. Phys.* **120**, 083903 (2016).
- [39] See the Supplemental Material at <http://link.aps.org/supplemental/10.1103/PhysRevApplied.16.034052> for lattice mismatching, various interface-stacking configurations, the resistance-area product formula, atomic-weight-projection band analysis, a comparison of VASP and QE for band calculations, the effect of SOC on GMR, and transport calculations in the presence of SOC. See also Refs. [23–25] therein.
- [40] R. Landauer, Spatial variation of currents and fields due to localized scatterers in metallic conduction, *IBM J. Res. Dev.* **1**, 223 (1957).
- [41] R. Landauer, Electrical resistance of disordered one-dimensional lattices, *Phil. Mag.* **21**, 863 (1970).
- [42] M. Büttiker, Y. Imry, R. Landauer, and S. Pinhas, Generalized many-channel conductance formula with application to small rings, *Phys. Rev. B* **31**, 6207 (1985).
- [43] T. Valet and A. Fert, Theory of perpendicular magnetoresistance in magnetic multilayers, *Phys. Rev. B* **48**, 7099 (1993).
- [44] J. Bass, CPP magnetoresistance of magnetic multilayers: A critical review, *J. Magn. Magn. Mater.* **408**, 244 (2016).
- [45] M. A. M. Gijs, J. B. Giesbers, M. T. Johnson, J. B. F. aan de Stegge, H. H. J. M. Janssen, S. K. J. Lenczowski, R. J. M. van de Veerdonk, and W. J. M. de Jonge, Perpendicular giant magnetoresistance of microstructures in Fe/Cr and Co/Cu multilayers, *J. Appl. Phys.* **75**, 6709 (1994).
- [46] T. Kubota, Z. Wen, and K. Takanashi, Current-perpendicular-to-plane giant magnetoresistance effects using Heusler alloys, *J. Magn. Magn. Mater.* **492**, 16567 (2019).
- [47] J. Sato, M. Oogane, H. Naganuma, and Y. Ando, Large magnetoresistance effect in epitaxial Co₂Fe_{0.4}Mn_{0.6}Si/Ag/Co₂Fe_{0.4}Mn_{0.6}Si devices, *Appl. Phys. Express* **4**, 113005 (2011).
- [48] Z. Wen, T. Kubota, Y. Ina, and K. Takanashi, Dual-spacer nanojunctions exhibiting large current-perpendicular-to-plane giant magnetoresistance for ultrahigh density magnetic recording, *Appl. Phys. Lett.* **110**, 102401 (2017).
- [49] W. Wang, A. Narayan, L. Tang, K. Dolui, Y. Liu, X. Yuan, Y. Jin, Y. Wu, I. Rungger, S. Sanvito, and F. Xiu, Spin-valve

- effect in NiFe/MoS₂/NiFe junctions, *Nano Lett.* **15**, 5261 (2015).
- [50] H. Lin, F. Yan, C. Hu, Q. Lv, W. Zhu, Z. Wang, Z. Wei, K. Chang, and K. Wang, Spin-valve effect in Fe₃GeTe₂/MoS₂/Fe₃GeTe₂ van der Waals heterostructures, *ACS Appl. Mater. Interfaces* **12**, 43921 (2020).
- [51] K. Dolui, A. Narayan, I. Rungger, and S. Sanvito, Efficient spin injection and giant magnetoresistance in Fe/MoS₂/Fe junctions, *Phys. Rev. B* **90**, 041401(R) (2014).
- [52] Y. Liu, P. Stradins, and S. H. Wei, Van der Waals metal-semiconductor junction: Weak Fermi level pinning enables effective tuning of Schottky barrier, *Sci. Adv.* **2**, e1600069 (2016).
- [53] A. N. Chantis, K. D. Belashchenko, E. Y. Tsymbal, and M. van Schilfgaarde, Tunneling Anisotropic Magnetoresistance Driven by Resonant Surface States: First-Principles Calculations on an Fe(001) Surface, *Phys. Rev. Lett.* **98**, 046601 (2007).
- [54] L. Gao, X. Jiang, S. H. Yang, J. D. Burton, E. Y. Tsymbal, and S. S. Parkin, Bias Voltage Dependence of Tunneling Anisotropic Magnetoresistance in Magnetic Tunnel Junctions with MgO and Al₂O₃ Tunnel Barriers, *Phys. Rev. Lett.* **99**, 226602 (2007).
- [55] S. Albarakati, C. Tan, Z.-J. Chen, J. G. Partridge, G. Zheng, L. Farrar, E. L. H. Mayes, M. R. Field, C. Lee, Y. Wang, M. Tian, F. Xiang, A. R. Hamilton, O. A. Tretiakov, D. Culcer, Y.-J. Zhao, and L. Wang, Antisymmetric magnetoresistance in van der Waals Fe₃GeTe₂/graphite/Fe₃GeTe₂ trilayer heterostructures, *Sci. Adv.* **5**, eaaw0409 (2019).
- [56] W. Park, D. V. Baxter, S. Steenwyk, I. Moraru, W. Pratt Jr, and J. Bass, Measurement of resistance and spin-memory loss (spin relaxation) at interfaces using sputtered current perpendicular-to-plane exchange-biased spin valves, *Phys. Rev. B* **62**, 1178 (2000).
- [57] R. Acharyya, H. Y. T. Nguyen, W. P. Pratt, and J. Bass, Spin-flipping associated with the antiferromagnet IrMn, *IEEE Trans. Magn.* **46**, 1454 (2010).